Facile Fabrication of Au Nanoparticles/Tin Oxide/Reduced Graphene Oxide Ternary Nanocomposite and Its High-Performance SF$_6$ Decomposition Components Sensing

Shoumiao Pi[1], Xiaoxing Zhang[1,2]*, Hao Cui[3], Dachang Chen[1], Guozhi Zhang[1], Song Xiao[1]* and Ju Tang[1]

[1] School of Electrical Engineering, Wuhan University, Wuhan, China, [2] Hubei Key Laboratory for High-Efficiency Utilization of Solar Energy and Operation Control of Energy Storage System, Hubei University of Technology, Wuhan, China, [3] State Key Laboratory of Power Transmission Equipment & System Security and New Technology, Chongqing University, Chongqing, China

A high-performance sensor for detecting SF$_6$ decomposition components (H$_2$S and SOF$_2$) was fabricated via hydrothermal method using Au nanoparticles/tin oxide/reduced graphene oxide (AuNPs-SnO$_2$-reduced graphene oxide [rGO]) hybrid nanomaterials. The sensor has gas-sensing properties that responded and recovered rapidly at a relatively low operating temperature. The structure and micromorphology of the prepared materials were characterized by X-ray diffraction (XRD), X-ray photoelectron spectroscopy (XPS), scanning electron microscopy (SEM), Raman spectroscopy, energy-dispersive spectroscopy (EDS), and Brunauer-Emmett-Teller (BET). The gas-sensing properties of AuNPs-SnO$_2$-rGO hybrid materials were studied by exposure to target gases. Results showed that AuNPs-SnO$_2$-rGO sensors had desirable response/recovery time. Compared with pure rGO (210/452 s, 396/748 s) and SnO$_2$/rGO (308/448 s, 302/467 s), the response/recovery time ratios of AuNPs-SnO$_2$-rGO sensors for 50 ppm H$_2$S and 50 ppm SOF$_2$ at 110°C were 26/35 s and 41/68 s, respectively. Furthermore, the two direction-resistance changes of the AuNPs-SnO$_2$-rGO sensor when exposed to H$_2$S and SOF$_2$ gas made this sensor a suitable candidate for selective detection of SF$_6$ decomposition components. The enhanced sensing performance can be attributed to the heterojunctions with the highly conductive graphene, SnO$_2$ films and Au nanoparticles.

Keywords: rGO, SF$_6$ decomposition components, gas sensor, tin oxide, hybrid nanomaterials

INTRODUCTION

Sulfur hexafluoride is widely used in gas-insulated switchgear (GIS) due to its excellent insulation and arc extinguishing performance (Ma et al., 2016). However, when partial discharge occurs in GIS due to equipment insulation defects, SF$_6$ gas decomposes and reacts with trace amounts of water and oxygen present in GIS, thus forming SOF$_2$, H$_2$S, SO$_2$, SO$_2$F$_2$, and other compounds (Derdouri et al., 1989; Vanbrunt and Herron, 1990; Casanovas et al., 1992; Tang et al., 2013). Studies revealed that the detection of these gas decomposition components can effectively judge the insulation defects to a certain extent, avoid the further development of the insulation defects, and prevent

the occurrence of serious insulation accidents (Tang et al., 2012, 2013; Li et al., 2014). Therefore, the development of high-performance detection technology for detecting SF$_6$ gas decomposition components has important scientific significance and high application value.

To date, many techniques have been successfully developed to detect SF$_6$ decomposition components, such as gas chromatography mass spectrometry technology (Koreh et al., 1997), infrared absorption spectroscopy technology (Kurte et al., 2001), photoacoustic spectroscopy technology (Luo et al., 2015) and gas sensor technology (Zhang et al., 2017). Among these techniques, the gas sensor method has received extensive attention due to its fast reaction speed, simple structure, and low production cost (Dai et al., 2011; Zhang et al., 2013, 2015). As a traditional gas-sensitive material, metal oxide has attracted the attention of many scholars because of its high response, fast response, and recovery speed. Its good sensing properties can be attributed to the unique properties of metal oxides, such as high-surface area to volume ratio, adjustable surface defects, and abundant active substances. To date, many metal oxide-based sensors have been developed to detect SF$_6$ decomposition components. For example, Liu et al. used NiO-modified zinc oxide to detect SO$_2$, SOF$_2$, and SO$_2$F$_2$ (Liu et al., 2017). Peng et al. used ZnO to detect SOF$_2$ (Peng et al., 2013) and Shao et al. used SnO$_2$-CuO to detect H$_2$S (Shao et al., 2013), which all showed high sensitivity and fast response speed. However, these sensors often operate at high temperatures, resulting in high-power consumption and integration difficulties. Therefore, development of SF$_6$ decomposition component detection sensors operating at a relatively low operating temperature has important significance.

Graphene exhibits excellent physical and chemical properties due to its unique two-dimensional structure and electronic properties, such as large specific surface area, extremely large carrier concentration, ultrahigh carrier mobility at room temperature, extremely low electrical noise, and good electron conduction rate (Novoselov, 2004; Ratinac et al., 2010; Chen et al., 2019; Li et al., 2019). Therefore, graphene has always been considered the most promising material for gas detection at a relatively low operating temperature (Schedin et al., 2007; Basu and Bhattacharyya, 2012). However, the intrinsic graphene surface lacks a dangling bond, which is considered as a key to chemisorption. A large number of studies have shown that intrinsic graphene has a good gas-sensitive response to only a few gases, such as NO$_2$ and NH$_3$ (Nomani et al., 2010; Pumera et al., 2010; Pearce et al., 2011). Subsequently, scholars have confirmed that graphene with certain defects or doping has strong response characteristics to specific gases, and the selectivity and sensitivity of graphene to specific gases can be improved by modifying graphene (Basu and Bhattacharyya, 2012; Gupta Chatterjee et al., 2015; Goutham et al., 2019). Zhang et al. constructed a novel gas sensor based on Au nanoparticles–reduced graphene oxide (rGO), exhibiting an enhanced sensing performance compared with intrinsic graphene for SF$_6$ decomposition components (Zhang et al., 2015). However, some disadvantages are observed, such as poor repeatability, long response and recovery time, etc.

To overcome these problems, some scholars have discovered in recent years that the combination of metal oxide and graphene can greatly improve the performance of gas sensors. Many different metal oxides, such as SnO$_2$, WO$_3$, and Cu$_2$O, have been successfully used in rGO modification and exhibited good-sensing properties for gases such as NO$_2$ and NH$_3$ (Deng et al., 2012; Mao et al., 2012; Kumar et al., 2015). During modification of graphene with metal oxides, SnO$_2$ has attracted considerable attention as a typical n-type wide band gap (3.6 eV) metal oxide semiconductor. Wang et al. successfully applied SnO$_2$ decorated reduced graphite oxide to detect the SF$_6$ decomposition components. The prepared sensor exhibited a response at −3.13% to 10 ppm SOF$_2$ at 125°C (Chu et al., 2018). Choi et al. revealed that sensors based on SnO$_2$ nanofibers–rGO nanocomposites can detect H$_2$S in low concentration at 200°C (Choi et al., 2014). However, the SF$_6$ decomposition component sensors mentioned above still have disadvantages, such as long recovery time and relatively high-operating temperature.

Furthermore, studies have found that the addition of noble metals such as Au, Pt, and Ag can greatly improve the sensing performance of gas sensors made of metal oxide and rGO composite films, in which noble metals behave as catalysts and thus the molecules break down into several active substances, which increases gas sensitivity (Kim et al., 2010; Choi et al., 2011; Cui et al., 2012). However, no research has attempted to fabricate sensors based on noble metal/metal oxide/graphene ternary nanocomposites to detect SF$_6$ decomposition components.

In this study, we used a hydrothermal synthesis method to prepare a novel sensor based on an AuNPs-SnO$_2$ nanoparticles-rGO (AuNPs-SnO$_2$-rGO) hybrid to detect the decomposition components of SF$_6$ and studied the gas-sensing performance of the sensor in detail. The experimental results showed that the sensor based on AuNPs-SnO$_2$-rGO exhibited excellent sensing performance after introduction of AuNPs. The response/recovery time for 50 ppm H$_2$S and 50 ppm SOF$_2$ at 110°C was (26/35 s, 41/68 s) and was greatly shortened.
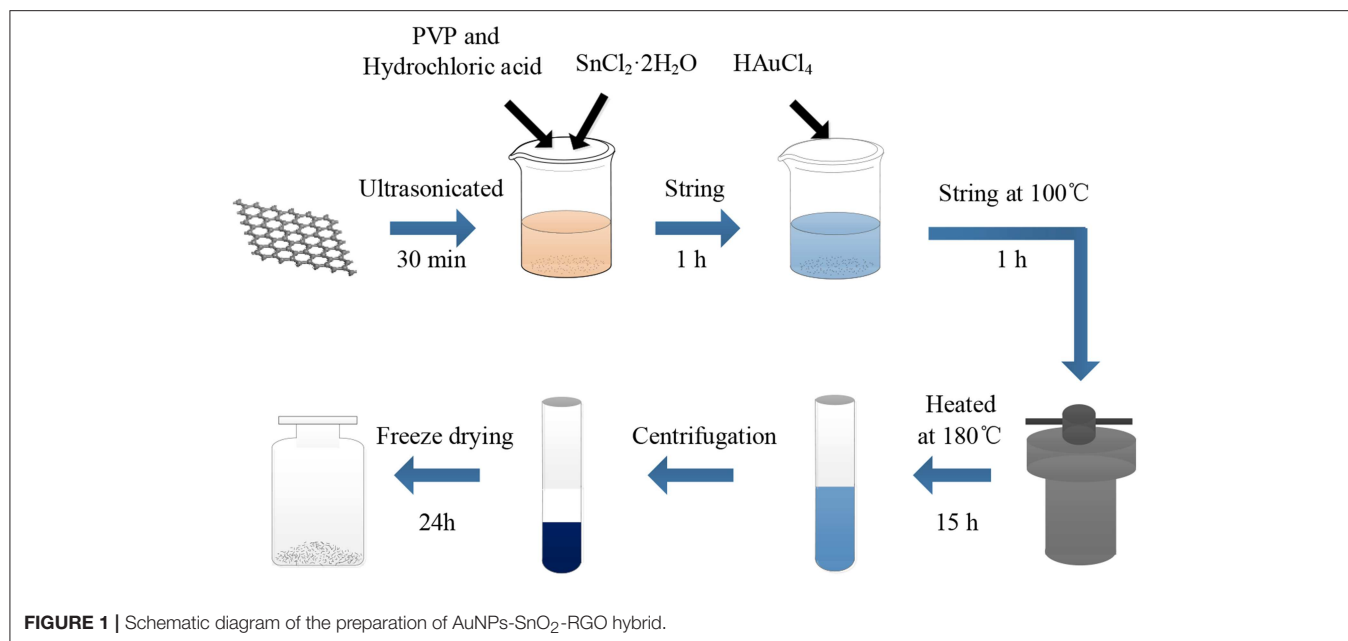
EXPERIMENTAL

Materials

Stannous chloride dihydrate (SnCl$_2$·2H$_2$O), polyvinylpyrrolidone (PVP, average molecular mass of 40,000 g/mol), and concentrated hydrochloric acid (HCl, 36–38%), tetrachloroauric acid (HAuCl$_4$) were purchased from Sinopharm Chemical Reagent Co., Ltd. (Shanghai, China). Graphene powder was purchased from Nanjing XFNANO Materials TECH Co., Ltd. (Nanjing, China). All reagents purchased were of analytical grade. Deionized water (DIW) was used as the solution in the experiment.

Preparation of AuNPs-SnO$_2$-rGO Nanocomposites

The graphene oxide (GO) employed in this study was prepared using a modified Hummer's method (Kovtyukhova et al., 1999). The AuNPs-SnO$_2$-rGO nanocomposites were prepared by a method similar to that described by Xu et al. (Zhang et al., 2011). The preparation is shown in **Figure 1**. In a typical synthesis,

FIGURE 1 | Schematic diagram of the preparation of AuNPs-SnO$_2$-RGO hybrid.

10 mg of GO was sonicated in 50 ml DIW for 30 min. Then, 0.5 ml HCl (36–38%), 100 mg PVP and 500 mg SnCl$_2$·2H$_2$O were added and stirred for 1 h at room temperature. Next, a certain amount of 0.01 M HAuCl$_4$ was added. The experimental solution was stirred at 100°C for 1 h. Then, the solution was placed into a Teflon-lined stainless-steel autoclave to react at 180°C for 15 h. After the autoclave was cooled down to room temperature, the above mixture was washed thrice with absolute ethanol and DIW, followed by freeze-drying for 24 h to prepare AuNPs-SnO$_2$-rGO hybrid powder for the subsequent experiment. Four different AuNPs-SnO$_2$-rGO samples were obtained at Au ratios of 0.5%, 1.5%, 2.5%, and 5% by weight. Similarly, the rGO, SnO$_2$, and SnO$_2$-rGO were also prepared.

Fabrication of Gas Sensors and Testing Method

The prepared material was dispersed in a mixture containing ionic water and isopropyl alcohol at a volume ratio of 1:1 at a concentration of 1 mg/ml and then ultrasonically treated for 30 min. The as-prepared AuNPs-SnO$_2$-rGO suspension was then drop-coated with a dropper onto a ceramic plate, which was coated with interdigital electrodes. The size of the interdigitated electrodes with a ceramic plate was 20 mm × 10 mm × 0.635 mm, and both the width and gaps of the 37 pairs of gold tracks on the electrode were 0.1 mm. Subsequently, the prepared sensor was placed in a dry box and dried at 60°C for 24 h to ensure stability before the test. To ensure the uniformity of the sensors prepared in a batch, we made three sensors for the same gas-sensing test, and the results are displayed in the form of reliable average. When the three results fluctuated little, we took the average of them to draw. When the three results fluctuated greatly, we rejected the outliers and retested. Gas sensors based on intrinsic graphene and tin oxide/graphene binary hybrid were prepared in the same manner for comparison.

The gas-sensing test system included the target gas, gas sample compounder, gas-sensing test chamber, electrochemical workstation, and exhaust gas treatment device (**Figure 2**). The entire experiment was based on a dynamic approach. The sensors were placed in a testing box inside a humidity cyclic chamber (Shanghai Shangqun Technology Co., Ltd.). The temperature in the humidity cyclic chamber was 25 ± 0.5°C. The temperature of the sensor was controlled by a heating electrode on the ceramic substrate. During the experiment, the gas to be tested was introduced through the air inlet and then mixed by the gas-sample compounder. When the sensor was in contact with the incoming gas, the change in resistance throughout the process was recorded by the electrochemical workstation. Due to the corrosive nature of the SF$_6$ decomposition components, there may be some changes in sensor parameters after prolonged exposure to these gases (Petrila et al., 2016; Bansode et al., 2017; Manikandan et al., 2018); however, the effects of such variations will not be discussed in this study. The gas flow rate was controlled to 500 ml/min. The resistance measurement interval was 2 s. The test voltage was 50 mV (AC), 1,000 Hz, and the heating voltage was 220 V, 50 Hz. Finally, we calculated the relative change in resistance (sensitivity) of the sensor based on the AuNPs-SnO$_2$-rGO hybrid, which is defined as

$$\Delta R/R(\%) = \frac{100 \times (R - R_0)}{R_0} \times 100\%,$$

where R refers to the resistance of the sensor in target gas, and R_0 represents the initial resistance of the sensor in dry air. The response time and recovery time are defined as the time to reach 90% of the total resistance change.

FIGURE 2 | Measurement system for gas sensing experimental.
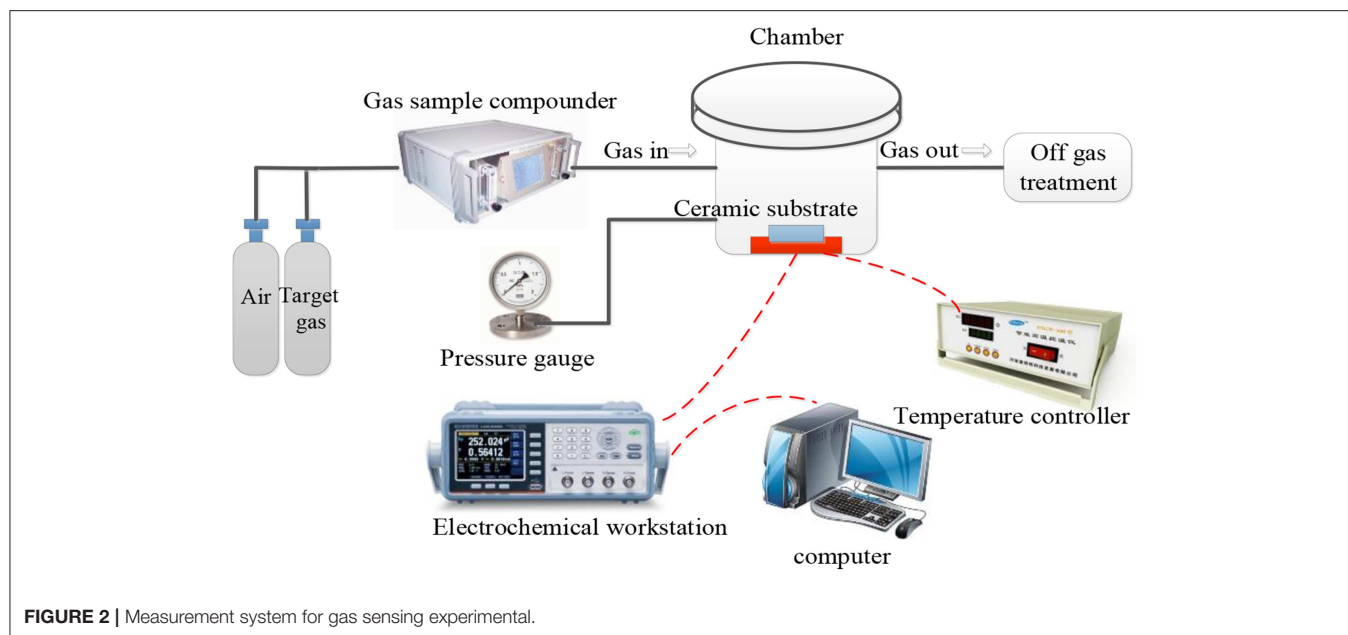
Instruments

The surface microstructure of the GO, SnO$_2$, and AuNPs-SnO$_2$-rGO hybrids was investigated by Zeiss SIGMA thermal field-emission scanning electron microscopy and energy dispersive spectroscopy (EDS) of QUANTA200 microscope at a 30 kV acceleration voltage. X-ray photoelectron spectroscopy (XPS) data of the AuNPs-SnO$_2$-rGO hybrid were obtained on a Thermo Scientific EscaLab 250Xi spectrometer. X-ray diffraction (XRD) was performed on a Bruker D8 Advance machine by using CuKα radiation (λ = 0.154 nm) with a wide range of scans from 10 to 90° and a speed of 10°/min. Raman spectroscopy data of GO and AuNPs-SnO$_2$-rGO hybrids were recorded on a LabRAM HORIBAHR800 Raman spectrometer with a laser with a wavelength of 632.8 nm. Resistance measurements in the experiments were performed using a CHI604E electrochemical workstation. The gas distribution was carried out using a GC500 dynamic gas distributor manufactured by Jiangsu Dong Fang Electric Technology Co., Ltd. (Jiangsu, China).

RESULTS AND DISCUSSION

Structure and Characterization Analysis

The structure of the AuNPs-SnO$_2$-rGO hybrids was examined by the XRD technique. The XRD results of GO and AuNPs-SnO$_2$-rGO are shown in **Figure 3**. Remarkably, GO exhibits a sharp diffraction peak at 2θ of 10.70° due to (002) diffraction of GO, indicating that most of the graphite powder are oxidized to GO (Liu et al., 2010). **Figure 3B** shows that the XRD pattern of the sample has obvious peak shape and smooth line, indicating that the crystal phase of AuNPs-SnO$_2$-rGO is well-formed. The XRD patterns of AuNPs-SnO$_2$-rGO nanocomposites reveal four highly diffractive peaks at 2θ of 26.61°, 33.89°, 37.95°, and 51.78° attributed to the (110), (101), (200), and (211) planes of SnO$_2$ (JCPDS 41-1445), respectively, indicating the successful

formation of SnO$_2$ crystals in the composite; this finding is similar to the work reported by Zhang et al. (2014). However, no obvious peak observed in the XRD pattern of AuNPs-SnO$_2$-rGO is attributable to Au, which may be due to the low content of Au nanoparticles in the nanocomposite (Zhang et al., 2011).

XPS measurement has proven to be an effective technique for detecting the elemental composition and chemical state of functional materials, especially for rGO-based materials. Therefore, we used XPS technology to characterize the prepared composite. **Figure 4A** is the Sn3d spectrum of the AuNPs-SnO$_2$-rGO ternary nanocomposite. As can be seen from the figure, two strong peaks occur at 486.36 and 494.81 eV, attributed to the binding energy of Sn3d$_{3/2}$ and Sn3d$_{5/2}$, respectively, indicating the SnO$_2$ formation (Khlayboonme and Thowladda, 2018; Nguyet et al., 2018). **Figure 4B** reveals the Au4f spectrum of the AuNPs-SnO$_2$-rGO hybrid, confirming the Au presence in the hybrids, with significant signals at 87.6 and 83.36 eV corresponding to metallic Au (Meng et al., 2017). Studies have shown that the C1s XPS spectrum can effectively estimate the chemical reduction level of GO. The C1s spectrum of the AuNPs-SnO$_2$-rGO hybrid in **Figure 4C** has four main parts, including sp^2 (~284.2 eV), sp^3 (~284.8 eV), C–O (~286. 7eV), and C=O (~288.5 eV). Sp^2 reflects the perfect standard structure of graphene, whereas sp^3 refers to the defects of graphene (Chen et al., 2018). Compared with the C1s spectrum of pristine GO in **Figure 4D**, the XPS peaks of the oxygen-containing functional groups C-O and C=O are severely weakened. Thus, GO has been successfully reduced in the hydrothermal synthesis.

The Raman spectra of GO and AuNPs-SnO$_2$-rGO are shown in **Figure 5**. Notably, Raman spectroscopy is an effective method for characterizing the structure of graphene substrate materials. Therefore, we further studied the existence of rGO in AuNPs-SnO$_2$-rGO nanocomposites by Raman spectroscopy in **Figure 5**. As reported in other studies, the D peak is mainly caused by
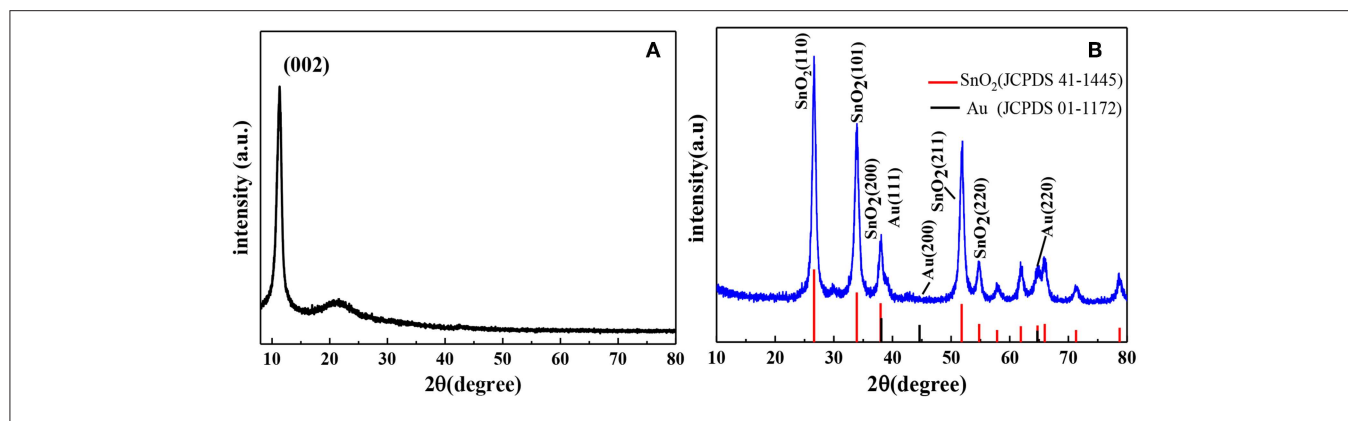
FIGURE 3 | XRD spectra of the samples: **(A)** GO, **(B)** AuNPs-SnO$_2$-rGO.
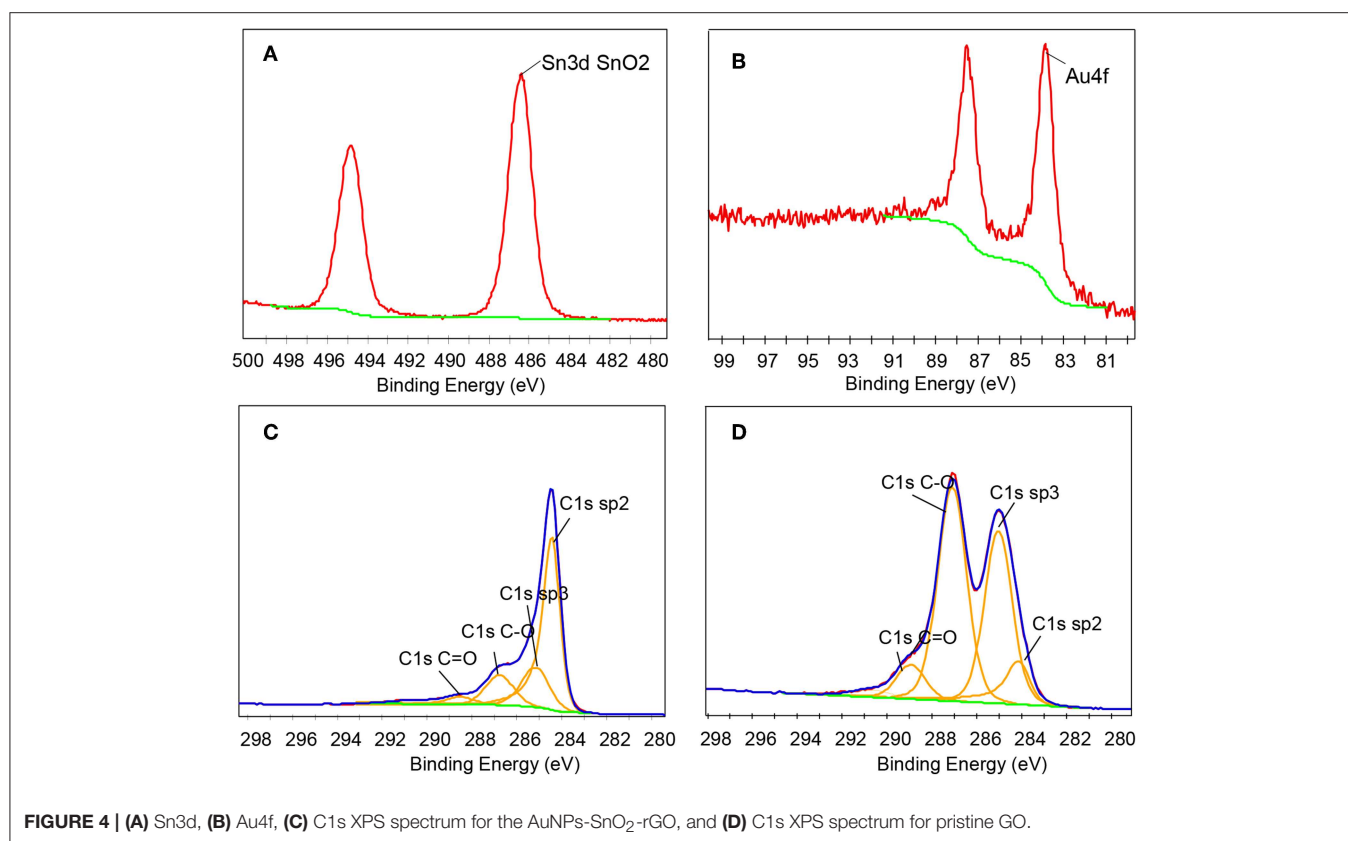

FIGURE 4 | (A) Sn3d, **(B)** Au4f, **(C)** C1s XPS spectrum for the AuNPs-SnO$_2$-rGO, and **(D)** C1s XPS spectrum for pristine GO.

the breathing-mode vibration of sp^3 carbon, which is generally considered the disordered vibration peak of graphene, which is used to characterize the structural defects or edges in graphene samples. This peak occurs at near 1,350 cm^{-1}. The G peak is considered the characteristic peak caused by the in-plane vibration of the sp^2 hybrid carbon atom, which occurs near 1,580 cm^{-1} (Stankovich et al., 2007; Ni et al., 2008; Malard et al., 2009; Dresselhaus et al., 2010). The Raman spectrum of GO in **Figure 5** shows two strong peaks at 1,588 and 1,341 cm^{-1}, corresponding to well-recorded G and D peaks. Although the Raman spectra of all samples showed G and D peaks,

they had some significant differences. Compared with the GO prepared under the same experimental conditions, the intensity ratio of the D band and the G band (ID/IG) of the AuNPs-SnO$_2$-rGO ternary is significantly increased, whereas the ID/IG reflects the defect density of graphene materials. The increase in ID/IG indicates the successful GO reduction in the AuNPs-SnO$_2$-rGO ternary nanocomposite. In addition, the increase in ID/IG may be due to a decrease in the sp^2 carbon domain, chemical bonds between the carbon matrix and AuNPs, and defects due to vacancies, grain boundaries and insertion of SnO$_2$ nanoparticles. All these observations indicate that we have
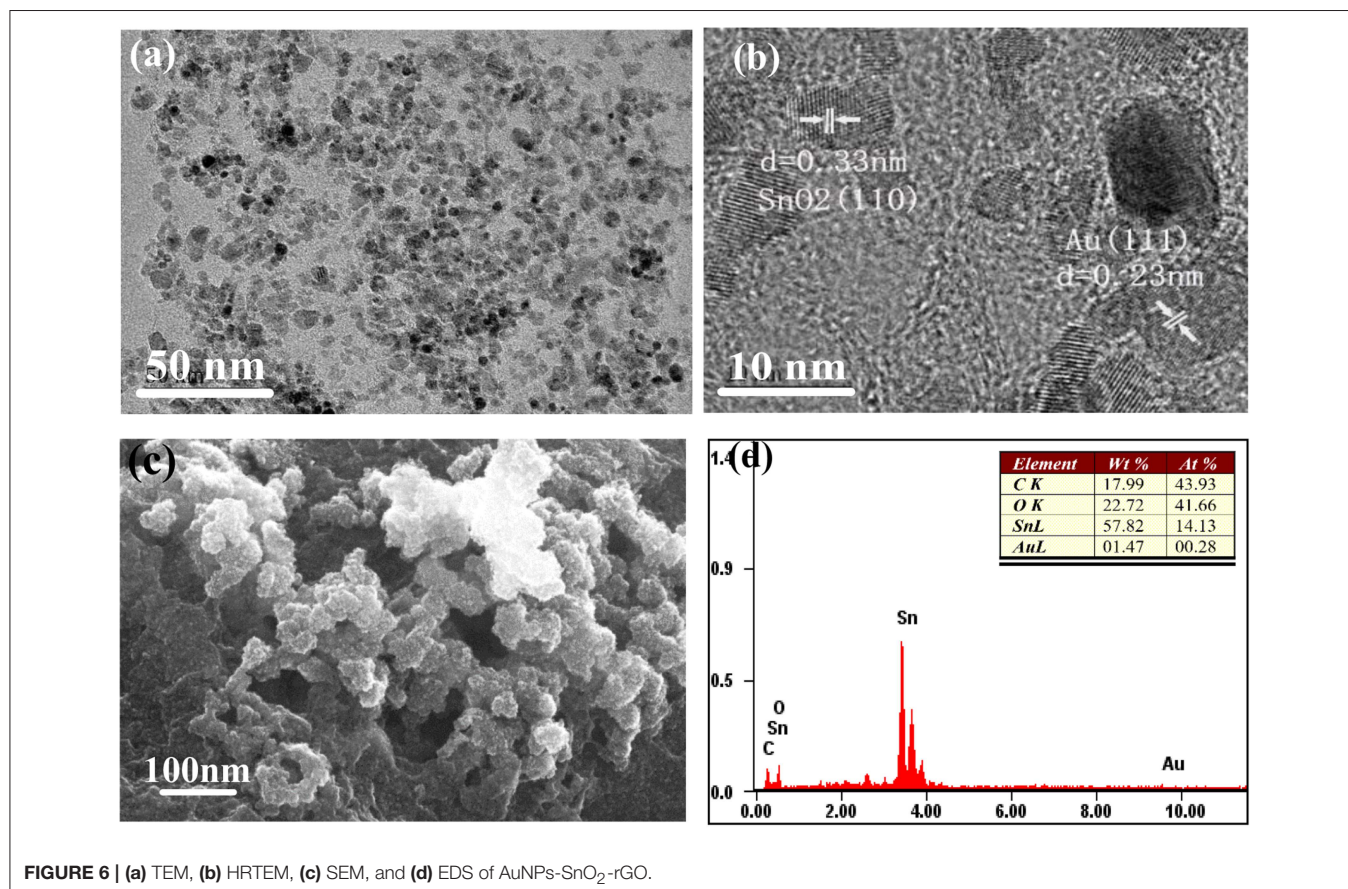
successfully formed the AuNPs-SnO$_2$-rGO ternary hybrid by hydrothermal treatment.
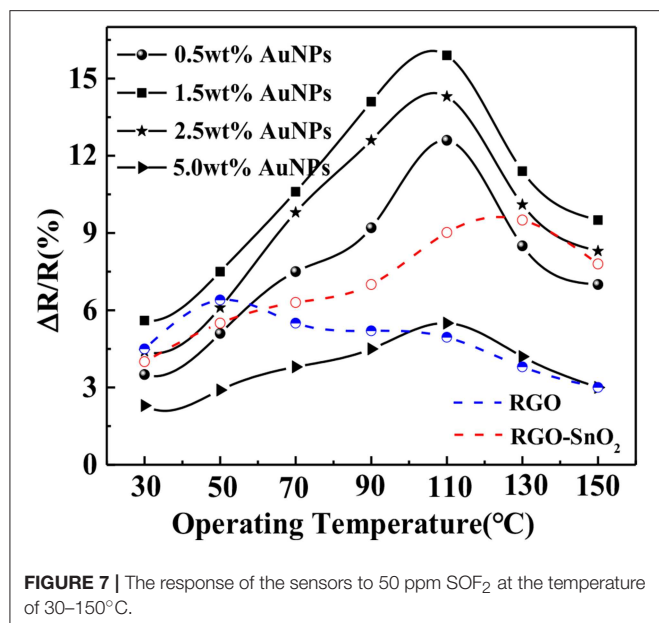
The morphology and structure of the AuNPs-SnO$_2$-rGO hybrid was further observed by TEM, HRTEM and SEM as shown in **Figure 6**. It can be observed from **Figure 6a** that

FIGURE 5 | Raman Shift of AuNPs-SnO$_2$-rGO and GO.
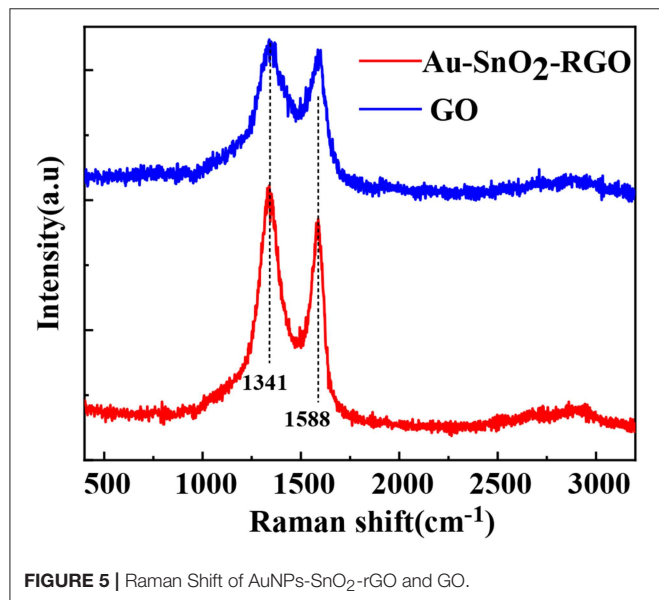
there are two kinds of nanoparticles with similar particle sizes uniformly dispersed on the surface of RGO. The HRTEM image (**Figure 6b**) shows an adjacent fringe spacing of 0.235 and 0.33 nm, which correspond to the (111) plane of Au and the (110) plane of SnO$_2$ crystal, respectively. The average diameter of the SnO$_2$ nanoparticles and the Au nanoparticles is about 5–7 nm. We can clearly see that a large amount of tin dioxide nanoparticles and Au nanoparticles are attached to the pleated rGO surface from a typical SEM image of AuNPs-SnO$_2$-rGO hybrid in **Figure 6c**. The EDS of AuNPs-SnO$_2$-rGO products is shown in **Figure 6d**, in which only Au, C, O, and Sn can be observed. This condition further confirms the successful doping of AuNPs and SnO$_2$ nanoparticles on the rGO surface, and the product is quite pure. Combined with XPS analysis, the composition of AuNPs-SnO$_2$-rGO hybrids is approximately 1.5% Au, 18% C, 58% Sn, 15.7% O in SnO$_2$ and 6.8% O in RGO.

The N$_2$ adsorption was performed to explore the architecture of the Au-SnO$_2$-RGO composite. The adsorption-desorption isotherms match the type IV based on the apparent hysteresis loops, which indicates the presence of a mesoporous structure (**Figure S1**). The surface areas of SnO$_2$-RGO and Au-SnO$_2$-RGO were calculated to be 84.58 and 106.35 m^{2}g^{-1}, respectively, using the Brunauer–Emmett–Teller (BET) model. It shows an average pore diameter of 3.38 nm for SnO$_2$-RGO and 3.29 nm for Au-SnO$_2$-RGO as calculated by the Barrett–Joyner–Halenda method (**Table S1**). The results show that the formation of the ternary

Element	Wt %	At %
C K	17.99	43.93
O K	22.72	41.66
SnL	57.82	14.13
AuL	01.47	00.28

FIGURE 6 | (a) TEM, **(b)** HRTEM, **(c)** SEM, and **(d)** EDS of AuNPs-SnO$_2$-rGO.

FIGURE 7 | The response of the sensors to 50 ppm SOF$_2$ at the temperature of 30–150°C.

composites significantly increases the surface area, which will greatly promote adsorption, thereby increasing the sensitivity of the sensors.

Sensing Performance of H$_2$S and SOF$_2$

We first investigated the effects of the proportion of chloroauric acid and the operating temperature on the sensing performance of the sensors. The sensing performance of all AuNPs-SnO$_2$-rGO-based sensors, SnO$_2$-rGO-based sensors and rGO-based sensors to 50 ppm SOF$_2$ was tested under the operating temperature ranging from 30 to 150°C. The test results are shown in **Figure 7**. The picture shows that 1.5 wt% AuNPs-SnO$_2$-rGO composite exhibited the maximum SOF$_2$-sensing response of 15.9% at an optimum operating temperature of 110°C. The optimal operating temperatures for SnO$_2$-rGO-based sensors and rGO-based sensors are 130 and 50°C, respectively. When chloroauric acid increased, the sensitivity to SOF$_2$ showed a tendency to increase slowly and then decrease. The reason for the analysis may be related to the large nanoparticles of AuNPs when great amount of chloroauric acid is added. For other SF$_6$ decomposition gases, the effect of AuNP addition ratio and the optimum operating temperature may be slightly different. However, considering the experiment consistency, we used this 1.5 wt% doping ratio sensor under the optimum operating temperature of 110°C in the next experiment.
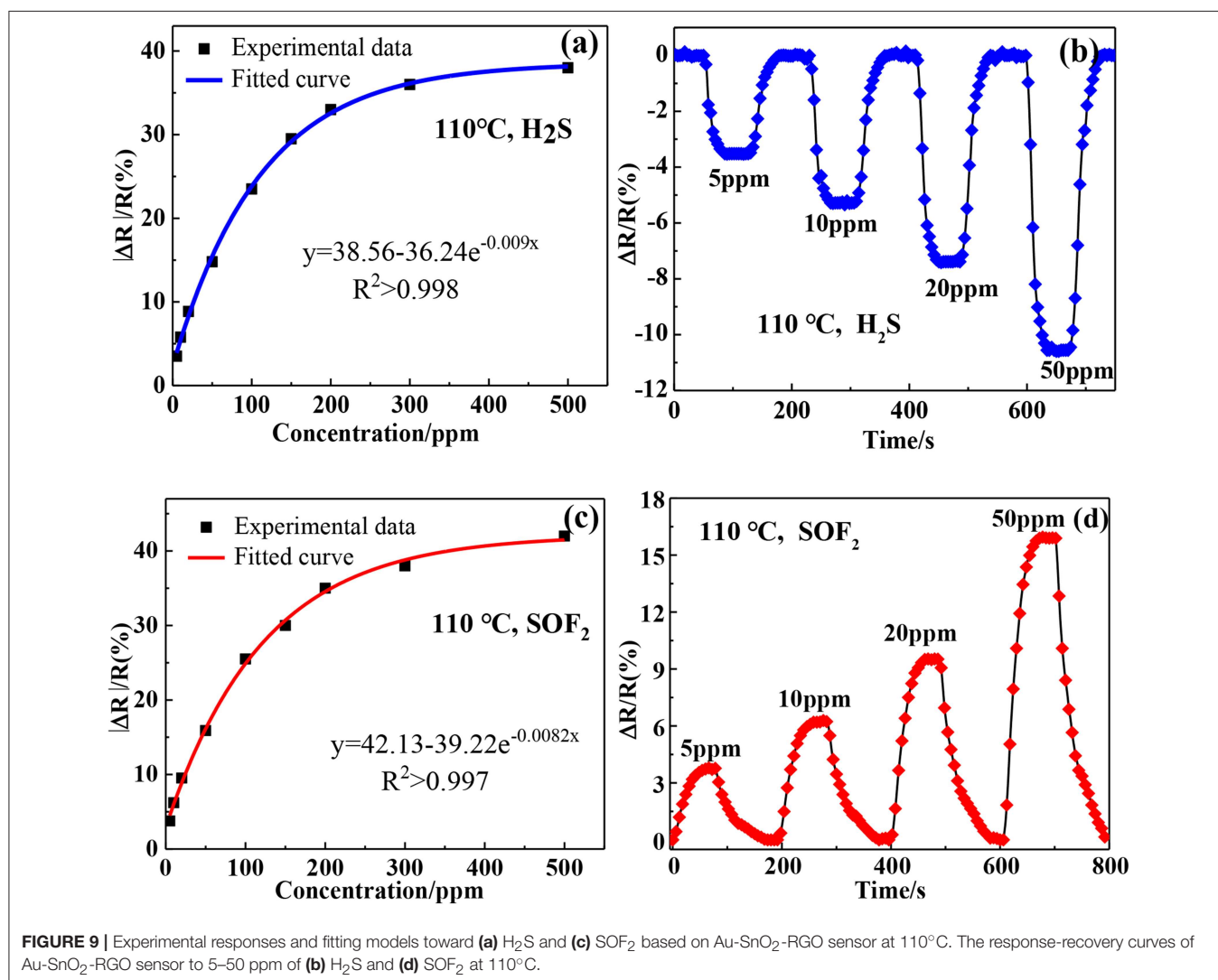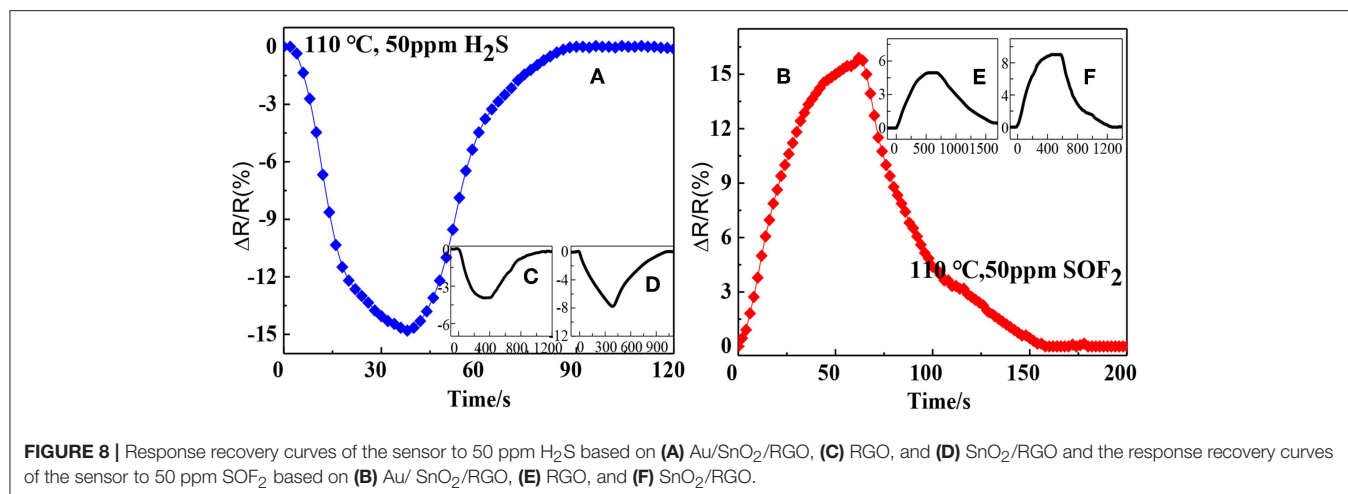
From the studies of Nakla et al. (2014) and Shao et al. (2013), we know that SnO$_2$ has poor sensing performance at low temperatures. Thus, we only discuss the characteristics of sensors based on intrinsic graphene, SnO$_2$-rGO, and AuNPs-SnO$_2$-rGO in this study.

Figure 8 illustrates the response and recovery curves of the rGO, SnO$_2$-rGO, and AuNPs-SnO$_2$-rGO-based sensors to 50 ppm H$_2$S and SOF$_2$ at 110°C. As can be seen from the figure, the response and recovery speeds are dramatically increased for the AuNPs-SnO$_2$-rGO sensor. When exposed to 50 ppm H$_2$S, the resistance of AuNPs-SnO$_2$-rGO sensor decreases rapidly, and the response, response time, and recovery time are −14.8%, 26 s, and 35 s (**Figure 8A**), respectively. Conversely, the rGO and SnO$_2$-rGO-based sensors show a slow drop in resistance after 50 ppm H$_2$S is introduced, with response and recovery times of rGO (210 s, 452 s) and SnO$_2$-rGO (308 s, 448 s) of both more than 4 min, respectively (**Figures 8C,D**). Furthermore, the resistance of the rGO sensor cannot return to its initial values. Interestingly, when exposed to 50 ppm SOF$_2$, the rGO, SnO$_2$-rGO, and AuNPs-SnO$_2$-rGO sensors all showed an increase in resistance, opposite to the H$_2$S-sensing behavior. This phenomenon allowed us to distinguish between the two gases. For 50 ppm SOF$_2$, the AuNPs-SnO$_2$-rGO sensor also has good sensing performance, and the response, response time, and recovery time are 15.9%, 41 s, and 68 s (**Figure 8B**), respectively. The response, response time, and recovery time of the rGO and SnO$_2$-rGO sensors for 50 ppm SOF$_2$ are relatively small and long (4.95%, 396 s, and 748 s) and (9.02%, 302 s, and 467 s), (**Figures 8E,F**). All these observations indicate that the sensor based on AuNPs-SnO$_2$-rGO hybrids not only increases the response compared with the sensor based on rGO and SnO$_2$-rGO for the detection of H$_2$S and SOF$_2$. Importantly, its detection response and recovery speed have been greatly improved from 8 min to 60 s.
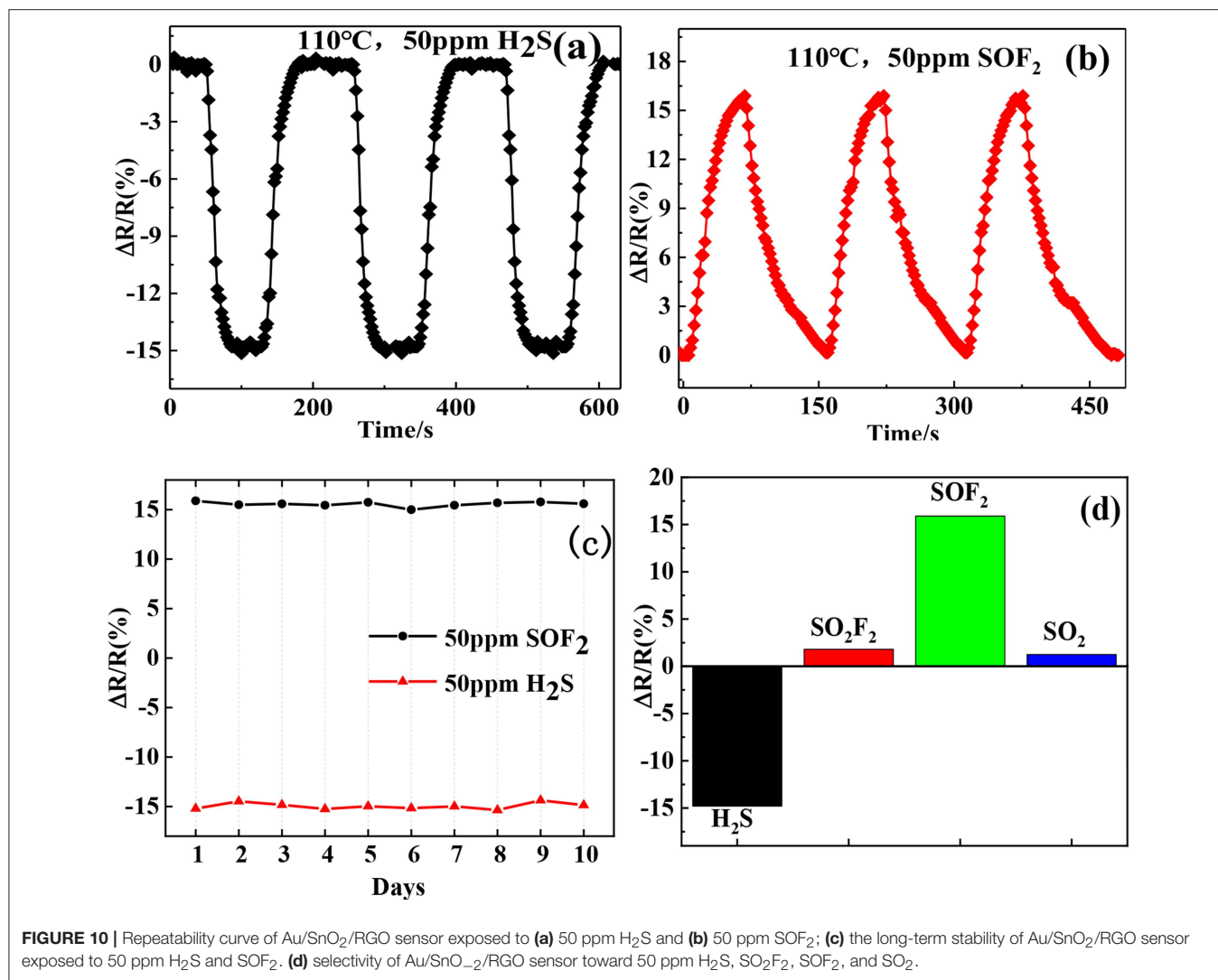
Figures 9a,c shows the relationship between the responses of Au-SnO$_2$-rGO sensor and gas concentrations at 110°C. Obviously, the response revealed an exponential trend with the increase of the target gas concentration. This result indicated that the adsorption of the target gas by the Au-SnO$_2$-rGO sensor almost reached saturation at higher concentrations. **Figures 9b,d** show that the response values of the Au-SnO$_2$-rGO-based sensors are orderly exposed to 5, 10, 20, and 50 ppm H$_2$S and SOF$_2$ at response values of H$_2$S −3.51, −5.78, −8.86, and −14.8% and SOF$_2$ of 3.77% 6.21, 9.52, and 15.9%, respectively. Clearly, the Au-SnO$_2$-rGO-based sensors respond quickly and reversibly to various concentrations of target gas, indicating that target gas can build a wide concentration detection range of H$_2$S and SOF$_2$ gas sensors at lower concentrations.

The repeatability and long-term stability of a sensor are important properties for practical applications. We repeatedly exposed the Au-SnO$_2$-rGO hybrid sensor to the 50 ppm H$_2$S and SOF$_2$ gas environment thrice. After each exposure, air was introduced to recover the sensor and then repeated alternately, as shown in **Figures 10a,b**. We can see clearly that the sensor exhibits a highly consistent response and recovery characteristics in three exposures, demonstrating good repeatability during the cycle test. Next, we conducted a 10-day long-term stability test, and the test results are shown in **Figure 10c**. The average and relative standard deviations of the response of the Au-SnO$_2$-rGO hybrid sensor at a testing concentration of 50 ppm of H$_2$S and SOF$_2$ for 10 days were (−14.68 and 2.1%) and (15.76 and 1.68%), respectively, exhibiting quite good long-term stability. Furthermore, we also evaluated the selectivity of the Au-SnO$_2$-rGO sensor to the typical decomposition components of SF$_6$ including H$_2$S, SO$_2$F$_2$, SOF$_2$, and SO$_2$. **Figure 10d** represents the sensor response of the Au-SnO$_2$-rGO-based sensor for 50 ppm of H$_2$S, SO$_2$F$_2$, SOF$_2$, and SO$_2$ at 110°C. Interestingly, the

FIGURE 8 | Response recovery curves of the sensor to 50 ppm H$_2$S based on (A) Au/SnO$_2$/RGO, (C) RGO, and (D) SnO$_2$/RGO and the response recovery curves of the sensor to 50 ppm SOF$_2$ based on (B) Au/ SnO$_2$/RGO, (E) RGO, and (F) SnO$_2$/RGO.

FIGURE 9 | Experimental responses and fitting models toward (a) H$_2$S and (c) SOF$_2$ based on Au-SnO$_2$-RGO sensor at 110°C. The response-recovery curves of Au-SnO$_2$-RGO sensor to 5–50 ppm of (b) H$_2$S and (d) SOF$_2$ at 110°C.

Au-SnO$_2$-rGO sensor exhibited a large response to H$_2$S and SOF$_2$ and had minimal response to SO$_2$F$_2$ and SO$_2$. Moreover, when exposed to H$_2$S, the sensor displayed a decrease in resistance.

However, after the SOF$_2$ was turned on, the sensor revealed a rise in resistance. This result allowed us to easily distinguish the two gases by the change in resistance. Therefore, the sensor based on

FIGURE 10 | Repeatability curve of Au/SnO$_2$/RGO sensor exposed to **(a)** 50 ppm H$_2$S and **(b)** 50 ppm SOF$_2$; **(c)** the long-term stability of Au/SnO$_2$/RGO sensor exposed to 50 ppm H$_2$S and SOF$_2$. **(d)** selectivity of Au/SnO$_{-2}$/RGO sensor toward 50 ppm H$_2$S, SO$_2$F$_2$, SOF$_2$, and SO$_2$.

the Au-SnO$_2$-rGO hybrid showed good selectivity for both H$_2$S and SOF$_2$ gases.

Water molecules may compete with target gas molecules during adsorption, thereby affecting gas adsorption. Therefore, the relative humidity effect is an important factor to be considered in sensor testing. **Figure 11** illustrates the response curves of the Au-SnO$_2$-rGO hybrid to 50 ppm H$_2$S and 50 ppm SOF$_2$ at different relative humidity. The gas sensor has relatively stable response in the range of 0-60% relative humidity, and the average response value and relative standard deviation are 14.74% (1.56%) and 15.84% (1.06%). However, when relative humidity exceeds 60%, the Au-SnO$_2$-rGO sensor's response to H$_2$S drops sharply. This result indicates that the Au-SnO$_2$-rGO hybrid sensor can operate in the 0–60% relative humidity range.

The sensing performances of the H$_2$S and SOF$_2$ sensors based on Au-SnO$_2$-rGO hybrids were also compared with the previously reported H$_2$S and SOF$_2$ sensors, as shown in **Table 1**. ZnO (Peng et al., 2013), CuO–ZnO (Xu et al., 2014), and NiO–ZnO (Liu et al., 2017) sensors responded quickly,

but they all worked above 200°C. Although the responses of PPy-WO$_3$ (Su and Peng, 2014) and Au-rGO (Zhang et al., 2015) sensors were higher than those of the Au-SnO$_2$-rGO sensors, the sensor in this work exhibited short response and recovery times. Compared with Wang et al. (Chu et al., 2018), our sensors can recover to the initial resistance in a very short time and work at relatively low operating temperature. Therefore, the huge advantage of the Au-SnO$_2$-rGO sensor was the fast response and recovery at relatively low operating temperature. Importantly, the selectivity of our Au-SnO$_2$-rGO sensor allowed for the differentiation of H$_2$S and SOF$_2$ when exposed to typical SF$_6$ decomposition components in GIS. All the above studies showed that our Au-SnO$_2$-rGO sensor had great advantages in the detection of SF$_6$ decomposition components in GIS.

Gas-Sensing Mechanism

The possible reasons for the superior sensor performance of the sensor are proposed as follows. (i) First, the most important

factor for good-sensing performance is the rGO presence. The excellent chemical and physical properties, such as large specific surface area, extremely large carrier concentration, and ultrahigh carrier mobility, provide possibility for the Au-SnO$_2$-rGO sensor to detect the H$_2$S and SOF$_2$ at a relatively low operating temperature. (ii) Second, Au-SnO$_2$-rGO is a resistance-type sensor from a macroscopic angle, wherein the principle is based on the conductance variations of the sensing element. The introduction of AuNPs and SnO$_2$ increases the electron transport rate of the sensing material, resulting in good sensing performance. (iii) The gas-sensitive response characteristics of the resistance-type sensor are closely related to the surface state of the adsorption substrate. The doping of AuNPs and SnO$_2$ significantly increases the number of active sites (such as defect sites and functional groups) on the graphene surface. Subsequently, these increased active sites facilitate gas adsorption and diffusion on the material surface. (iv) The introduction of AuNPs and SnO$_2$ results in the formation of new heterojunctions

between the various components in the sensing material. In SnO$_2$-rGO, the p-n heterojunction formed between SnO$_2$ and rGO plays an important role in improving the sensing performance of rGO-based sensors. Scholars have proved that due to the difference in work function between n-type SnO$_2$ (4.55 eV) and p-type rGO (4.75 eV), when the two are in contact, the electrons will flow from SnO$_2$ to rGO, establishing the electron depletion region (Mao et al., 2012). In ambient air, the formations of chemisorbed ionized oxygen (O$_2^-$) on the surface of SnO$_2$ and rGO result in a further alternation in the electron depletion region due to electron transfer from the SnO$_2$-rGO to oxygen in a manner similar to that previously reported literature (Lu et al., 2010). When exposed to the target gases (such as H$_2$S and SOF$_2$), the gas molecules can be easily adsorbed on the active site of the composite and react with the pre-adsorbed oxygen. Thus, the electrons trapped in the chemisorbed-ionized oxygen transfer between the sensing material and gas molecules, resulting in a modification of the electron depletion layer at the
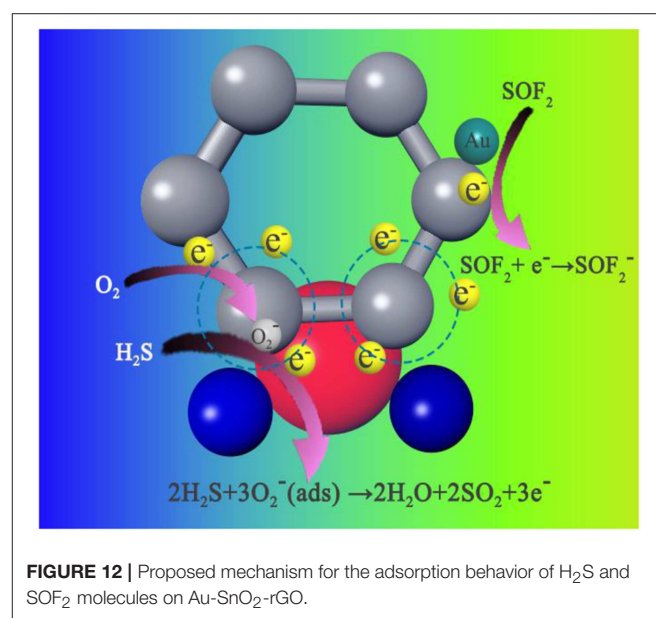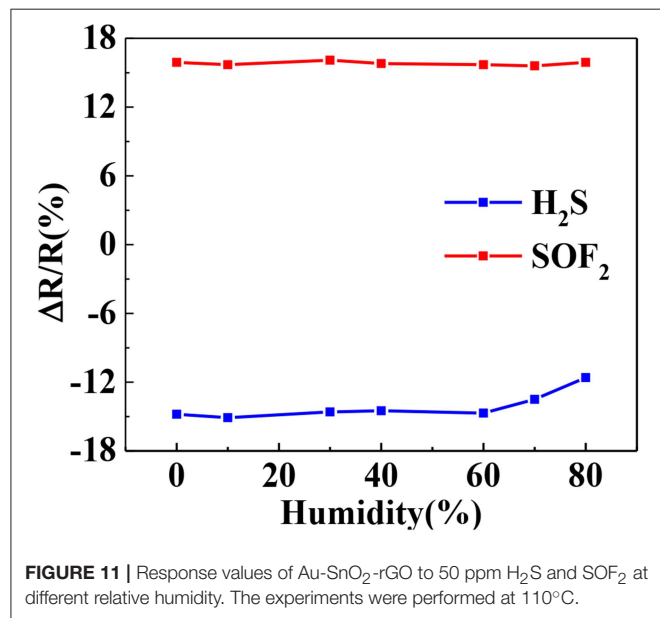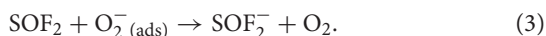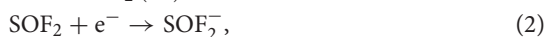

FIGURE 11 | Response values of Au-SnO$_2$-rGO to 50 ppm H$_2$S and SOF$_2$ at different relative humidity. The experiments were performed at 110°C.

FIGURE 12 | Proposed mechanism for the adsorption behavior of H$_2$S and SOF$_2$ molecules on Au-SnO$_2$-rGO.
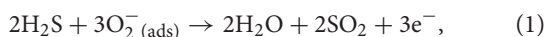
TABLE 1 | Comparison of H$_2$S and SOF$_2$ sensing performances of our proposed sensor with other published sensors.

Materials	Gas species	Concentrations (ppm)	Operating temperature	Response	Response/recovery time(s/s)	References
CuO-ZnO	H$_2$S	2	225	1,035%	30/98	Xu et al., 2014
ZnO	SOF$_2$	10	300	7%	10/17	Peng et al., 2013
NiO-ZnO	SOF$_2$	100	260	22.25	18/22	Liu et al., 2017
PPy-WO$_3$	H$_2$S	1	RT	81%	360/12600	Su and Peng, 2014
Au-rGO	H$_2$S	100	RT	−28.15%	—	Zhang et al., 2015
	SOF$_2$	100	RT	23.83%	—	
SnO$_2$-rGO	H$_2$S	100	125	33.02%	209/900	Chu et al., 2018
	SOF$_2$	10	125	−3.24%	255/330	
Au- SnO$_2$-rGO	H$_2$S	50	110	−14.8%	26/35	This work
	SOF$_2$	50	110	15.9%	41/68	

SnO$_2$ and rGO interfaces. The surface reaction between the H$_2$S and SOF$_2$ molecules and chemisorbed-ionized oxygen can be proposed as follows (Su and Peng, 2014; Chu et al., 2018):

$$2H_2S + 3O_2^-{}_{(ads)} \rightarrow 2H_2O + 2SO_2 + 3e^-, \qquad (1)$$

$$SOF_2 + e^- \rightarrow SOF_2^-, \qquad (2)$$

$$SOF_2 + O_2^-{}_{(ads)} \rightarrow SOF_2^- + O_2. \qquad (3)$$

In addition, the introduction of AuNPs may lead to the formation of a nano-Sttocky contact between AuNPs and p-type rGO or n-type SnO$_2$. AuNPs can dissociate and chemically adsorb O$_2$ under ambient air. Therefore, an electron depletion region is formed around the AuNPs by oxygen adsorption. The work function of these regions is higher than the work function of the SnO$_2$ nanoparticles (Meng et al., 2018). This condition results in the formation of a nano-Sttocky contact at the Au–SnO$_2$ interface and electron transfer from SnO$_2$ and rGO to AuNPs. This phenomenon eventually leads to rapid changes in resistance and high sensitivity. (v) Enhanced sensing performance was obtained by the "chemical mechanism" due to the introduction of AuNPs. The "chemical mechanism" proposes that AuNPs activate and decompose molecular oxygen, and its atomic product is then diffused to the SnO$_2$ carrier by a spillover effect. This process greatly increases the amount of oxygen that can refill the SnO$_2$ surface vacancies and the rate at which this refill occurs, thereby extracting electrons from SnO$_2$ quickly at low temperatures (Cui et al., 2012).

In **Figure 12**, we propose a possible mechanism for the Au-SnO$_2$-rGO sensor selectivity to distinguish between H$_2$S and SOF$_2$. In general, H$_2$S is a typical reducing gas (Su and Peng, 2014; Wan et al., 2018). When the Au-SnO$_2$-rGO sensor is exposed to H$_2$S, electrons trapped by the chemisorbed-ionized oxygen will be released into the conduction band according to formula (1). This phenomenon results in the width of the electron depletion layer to be narrowed, thereby causing a decrease in resistance. By contrast, when exposed to the SOF$_2$ gas, the electrons are transferred from the Au-SnO$_2$-rGO to the SOF$_2$ as shown in formulas (2) and (3). Thus, the electron carrier concentration is decreased, whereby the resistance of the gas sensor is increased.

CONCLUSION

In this study, a high-performance sensor for the detection of H$_2$S and SOF$_2$ has been successfully fabricated by employing Au-SnO$_2$-rGO hybrids as sensing materials, which were prepared by hydrothermal synthesis. The gas-sensing properties of AuNPs-SnO$_2$-rGO hybrid materials were studied by exposure to target gases. The main conclusions we got are as follows:

(1) The introduction of AuNPs in SnO$_2$-rGO hybrids significantly improves the sensing properties of the sensors to H$_2$S and SOF$_2$ at relatively low operating temperature, compared with SnO$_2$-rGO hybrids.
(2) AuNPs-SnO$_2$-rGO sensors had desirable response/recovery time. The response time of Au-SnO$_2$-rGO to 50 ppm H$_2$S and SOF$_2$ at 110°C is (26, 35 s) and (41, 68 s).
(3) The sensor has the ability to select four typical decomposition products of SF$_6$ and shows the potential to distinguish between H$_2$S and SOF$_2$ from the direction of resistance change. The AuNPs-SnO$_2$-rGO hybrid provides a new sensing material for the manufacture of high-performance SF$_6$ decomposition product-detection sensors at a low operating temperature.
(4) The enhanced sensing performance can be attributed to the heterojunctions with the highly conductive graphene, SnO$_2$ films, and Au nanoparticles.

DATA AVAILABILITY

All datasets generated for this study are included in the manuscript and/or the **Supplementary Files**.

AUTHOR CONTRIBUTIONS

XZ designed and guided this investigation. SP performed this study and wrote this paper. DC, HC, GZ, SX, and JT implemented the modification of this paper in order to improve its quality. All authors read and approved the final manuscript.

ACKNOWLEDGMENTS

SUPPLEMENTARY MATERIAL

The Supplementary Material for this article can be found online at: https://www.frontiersin.org/articles/10.3389/fchem.2019.00476/full#supplementary-material

REFERENCES

Bansode, S. R., Khare, R. T., Jagtap, K. K., More, M. A., and Koinkar, P. (2017). One step hydrothermal synthesis of SnO2-RGO nanocomposite and its field emission studies. *Mater. Sci. Semiconduct. Proc.* 63, 90–96. doi: 10.1016/j.mssp.2017.02.013

Basu, S., and Bhattacharyya, P. (2012). Recent developments on graphene and graphene oxide based solid state gas sensors. *Sens. Actuat. B Chem.* 173, 1–21. doi: 10.1016/j.snb.2012.07.092

Casanovas, A., Casanovas, J., Lagarde, F., and Belarbi, A. (1992). Study of the decomposition of SF6 under DC negative polarity corona discharges (point to plane geometry): influence of the metal constituting the plane electrode. *J. Appl. Phys.* 72, 3344–3354. doi: 10.1063/1.351456

Chen, D., Tang, J., Zhang, X., Fang, J., Li, Y., and Zhuo, R. (2018). Detecting decompositions of sulfur hexafluoride using reduced graphene oxide decorated with Pt nanoparticles. *J. Phys. D Appl. Phys.* 51:185304. doi: 10.1088/1361-6463/aaba95

Chen, D., Zhang, X., Tang, J., Cui, Z., and Cui, H. (2019). Pristine and Cu decorated hexagonal InN monolayer, a promising candidate to detect and scavenge SF$_6$ decompositions based on first-principle study. *J. Hazard. Mater.* 363, 346–357. doi: 10.1016/j.jhazmat.2018.10.006

Choi, S.-J., Jang, B.-H., Lee, S.-J., Min, B. K., Rothschild, A., and Kim, I.-D. (2014). Selective detection of acetone and hydrogen sulfide for the diagnosis of diabetes and halitosis using SnO2 nanofibers functionalized with reduced graphene oxide nanosheets. *ACS Appl. Mater. Interfaces* 6, 2588–2597. doi: 10.1021/am405088q

Choi, S. W., Jung, S. H., and Kim, S. S. (2011). Functionalization of selectively grown networked SnO2 nanowires with Pd nanodots by ray radiolysis. *Nanotechnology* 22:225501. doi: 10.1088/0957-4484/22/22/225501

Chu, J., Wang, X., Wang, D., Yang, A., Lv, P., Wu, Y., et al. (2018). Highly selective detection of sulfur hexafluoride decomposition components H2S and SOF2, employing sensors based on tin oxide modified reduced graphene oxide. *Carbon* 135, 95–103. doi: 10.1016/j.carbon.2018.04.037

Cui, S., Pu, H., Mattson, E. C., Lu, G., Mao, S., Weinert, M., et al. (2012). Ag nanocrystal as a promoter for carbon nanotube-based room-temperature gas sensors. *Nanoscale* 4, 5887–5894. doi: 10.1039/c2nr31556d

Dai, H., Xiao, P., and Lou, Q. (2011). Application of SnO2/MWCNTs nanocomposite for SF6 decomposition gas sensor. *Phys. Status Solidi Appl. Mater.* 208, 1714–1717. doi: 10.1002/pssa.201026562

Deng, S., Tjoa, V., Fan, H. M., Tan, H. R., Sayle, D. C., Olivo, M., et al. (2012). Reduced graphene oxide conjugated Cu2O nanowire mesocrystals for high-performance NO2 gas sensor. *J. Am. Chem. Soc.* 134, 4905–4917. doi: 10.1021/ja211683m

Derdouri, A., Casanovas, J., Hergli, R., Grob, R., and Mathieu, J. (1989). Study of the decomposition of wet SF6, subjected to 50-Hz ac corona discharges. *J. Appl. Phys.* 65, 1852–1857. doi: 10.1063/1.342919

Dresselhaus, M. S., Jorio, A., Hofmann, M., Dresselhaus, G., and Saito, R. (2010). Perspectives on carbon nanotubes and graphene Raman spectroscopy. *Nano Lett.* 10, 751–758. doi: 10.1021/nl904286r

Goutham, S., Jayarambabu, N., Sandeep, C., Sadasivuni, K. K., Kumar, D. S., and Rao, K. V. (2019). Resistive room temperature LPG sensor based on a graphene/CdO nanocomposite. *Microchim. Acta* 186:62. doi: 10.1007/s00604-018-3170-2

Gupta Chatterjee, S., Chatterjee, S., Ray, A. K., and Chakraborty, A. K. (2015). Graphene-metal oxide nanohybrids for toxic gas sensor: a review. *Sens. Actuat. B Chem.* 221, 1170–1181. doi: 10.1016/j.snb.2015.07.070

Khlayboonme, S. T., and Thowladda, W. (2018) Synthesis and characterization of Cu-doped SnO2 thin films by aerosol pyrolysis technique for gas sensor application. *Key Eng. Mater.* 766, 205–210. doi: 10.4028/www.scientific.net/KEM.766.205

Kim, S. S., Park, J. Y., Choi, S. W., Kim, H. S., Na, H. G., Yang, J. C., et al. (2010). Significant enhancement of the sensing characteristics of In2O3 nanowires by functionalization with Pt nanoparticles. *Nanotechnology* 21:415502. doi: 10.1088/0957-4484/21/41/415502

Koreh, O., Rikker, T., Molnar, G., Mahara, B. M., Torkos, K., and Borossay, J. (1997). Study of decomposition of sulphur hexafluoride by gas chromatography mass spectrometry. *Rapid Commun. Mass Spectr.* 11, 1643–1648.

Kovtyukhova, N. I., Ollivier, P. J., Martin, B. R., Mallouk, T. E., Chizhik, S. A., Buzaneva, E. V., et al. (1999). Layer-by-layer assembly of ultrathin composite films from micron sized graphite oxide sheets and polycations. *Chem. Mater.* 11, 771–778. doi: 10.1021/cm981085u

Kumar, N., Srivastava, A. K., Patel, H. S., Gupta, B. K., and Varma, G. D. (2015). Facile synthesis of ZnO-reduced graphene oxide nanocomposites for NO2 gas sensing applications. *Eur. J. Inorg. Chem.* 2015, 1912–1923. doi: 10.1002/ejic.201403172

Kurte, R., Heise, H. M., and Klockow, D. (2001). Quantitative infrared spectroscopic analysis of SF6 decomposition products obtained by electrical partial discharges and sparks using PLS-calibrations. *J. Mol. Struct.* 565, 505–513. doi: 10.1016/S0022-2860(00)00847-4

Li, B., Li, M., Meng, F., and Liu, J. (2019). Highly sensitive ethylene sensors using Pd nanoparticles and rGO modified flower-like hierarchical porous α-Fe2O3. *Sens. Actuat. B Chem.* 290, 396–405. doi: 10.1016/j.snb.2019.04.002

Li, Q., Cong, H., Xing, J., Qi, B., and Li, C. (2014). On-line temperature monitoring of the GIS contacts based on infrared sensing technology. *J. Electr. Eng. Technol.* 9, 1385–1393. doi: 10.5370/JEET.2014.9.4.1385

Liu, H., Zhou, Q., Zhang, Q., Hong, C., Xu, L., Jin, L., et al. (2017). Synthesis, characterization and enhanced sensing properties of a NiO/ZnO p-n junctions sensor for the SF6 decomposition byproducts SO2, SO2F2, and SOF2. *Sensors* 17:913. doi: 10.3390/s17040913

Liu, S., Tian, J., Wang, L., Li, H., Zhang, Y., and Sun, X. (2010). Stable aqueous dispersion of graphene nanosheets: noncovalent functionalization by a polymeric reducing agent and their subsequent decoration with Ag nanoparticles for enzymeless hydrogen peroxide detection. *Macromolecules* 43, 10078–10083. doi: 10.1021/ma102230m

Lu, G., Ocola, L. E., and Chen, J. (2010). Gas sensors: room-temperature gas sensing based on electron transfer between discrete tin oxide nanocrystals and multiwalled carbon nanotubes. *Adv. Mater.* 21, 2487–2491. doi: 10.1002/adma.200803536

Luo, J., Fang, Y. H., Su, Z. X., Li, D. C., Zhao, Y. D., Wang, A. J., et al. (2015). The research of temperature properties of photoacoustic spectroscopy detection for SF6 decomposition products in gas insulated switchgear. *Anal. Methods* 7, 3806–3813. doi: 10.1039/C5AY00585J

Ma, G., Wu, Z., Zhou, H., Jiang, J., Chen, W., Zheng, S., et al. (2016). A wireless and passive online temperature monitoring system for GIS based on Surface-Acoustic-Wave sensor. *IEEE Trans. Power Deliver.* 31, 1270–1280. doi: 10.1109/TPWRD.2015.2482985

Malard, L. M., Pimenta, M. A., Dresselhaus, G., and Dresselhaus, M. S. (2009). Raman spectroscopy in graphene. *Phys. Rep.* 473, 51–87. doi: 10.1016/j.physrep.2009.02.003

Manikandan, V., Iulian, P., Vigneselvan, S., Dharmavarapu, R., Juodkazis, S., Kavita, S., et al. (2018). Efficient humidity-sensitive electrical response of annealed lithium substituted nickel ferrite (Li-NiFe2O4) nanoparticles under ideal, real and corrosive environments. *J. Mater. Sci. Mater. Electr.* 29, 18660–18667. doi: 10.1007/s10854-018-9987-y

Mao, S., Cui, S., Lu, G., Yu, K., Wen, Z., and Chen, J. (2012). Tuning gas-sensing properties of reduced graphene oxide using tin oxide nanocrystals. *J. Mater. Chem.* 22, 11009–11013. doi: 10.1039/c2jm30378g

Meng, F., Zheng, H., Chang, Y., Zhao, Y., Li, M., Wang, C., et al. (2018). One-step synthesis of Au/SnO2/RGO nanocomposites and their VOC sensing properties. *IEEE Trans. Nanotechnol.* 17, 212–219. doi: 10.1109/TNANO.2017.2789225

Meng, F., Zheng, H., Sun, Y., Li, M., and Liu, J. (2017). Trimethylamine sensors based on Au modified hierarchical porous single-crystalline ZnO nanosheets. *Sensors* 1:E1478. doi: 10.3390/s17071478

Nakla, W., Wisitsora-at, A., Tuantranont, A., Singjai, P., and Phanichphant, S., iewhiran C. (2014). H2S sensor based on SnO2 nanostructured film prepared by high current heating. *Sens. Actuat. B Chem.* 203, 565–578. doi: 10.1016/j.snb.2014.07.021

Nguyet, Q. T. M., Duy, N. V., Hung, C. M., Hoa, N. D., and Van Hieu, N. (2018). Ultrasensitive NO2 gas sensors using hybrid heterojunctions of multi-walled carbon nanotubes and on-chip grown SnO2 nanowires. *J. Appl. Phys. Lett.* 112:153110. doi: 10.1063/1.5023851

Ni, Z., Wang, Y., Yu, T., and Shen, Z. (2008). Raman spectroscopy and imaging of graphene. *Nano Res.* 1, 273–291. doi: 10.1007/s12274-008-8036-1

Nomani, M. W. K., Shishir, R., Qazi, M., Diwan, D., Shields, V. B., Spencer, M. G., et al. (2010). Highly sensitive and selective detection of NO2 using epitaxial graphene on 6H-SiC. *Sens. Actuat. B Chem.* 150, 301–307. doi: 10.1016/j.snb.2010.06.069

Novoselov, K. S. (2004). Electric field effect in atomically thin carbon films. *Science* 306, 666–669. doi: 10.1126/science.1102896

Pearce, R., Iakimov, T., Andersson, M., Hultman, L., Spetz, A. L., and Yakimova, R. (2011). Epitaxially grown graphene-based gas sensors for ultra-sensitive NO2 detection. *Sens. Actuat. B* 155, 451–455. doi: 10.1016/j.snb.2010.12.046

Peng, S., Wu, G., Song, W., and Wang, Q. (2013). Application of flower-like ZnO nanorods gas sensor detecting SF6 decomposition products. *J Nanomater.* 2013:135147. doi: 10.1155/2013/135147

Petrila, I., Popa, K., and Tudorache, F. (2016). Microstructure, electrical and humidity sensing properties of light rare earths zirconates. *Sens. Actuat. A Phys.* 247, 156–161. doi: 10.1016/j.sna.2016.05.039

Pumera, M., Ambrosi, A., Bonanni, A., Chng, E. L. K., and Poh, H. L. (2010). Graphene for electrochemical sensing and biosensing. *Trends Anal. Chem.* 29, 954–965. doi: 10.1016/j.trac.2010.05.011

Ratinac, K. R., Yang, W., Ringer, S. P., and Braet, F. (2010). Toward ubiquitous environmental gas sensors-capitalizing on the promise of graphene. *Environ. Sci. Technol.* 44, 1167–1176. doi: 10.1021/es902659d

Schedin, F., Geim, A. K., Morozov, S. V., Hill, E. W., Blake, P., and Katsnelson, M. (2007). Detection of individual gas molecules adsorbed on graphene. *Nat. Mater.* 6, 652–655. doi: 10.1038/nmat1967

Shao, F., Hoffmann, M. W. G., Prades, J. D., Zamani, R., Arbiol, J., Morante, J. R., et al. (2013). Heterostructured p-CuO (nanoparticle)/n-SnO2 (nanowire) devices for selective H2S detection. *Sens. Actuat. B Chem.* 181, 130–135. doi: 10.1016/j.snb.2013.01.067

Stankovich, S., Dikin, D. A., Piner, R. D., Kohlhaas, K. A., Kleinhammes, A., Jia, Y., et al. (2007). Synthesis of graphene-based nanosheets via chemical reduction of exfoliated graphite oxide. *Carbon* 45, 1558–1565. doi: 10.1016/j.carbon.2007.02.034

Su, P., and Peng, Y. (2014). Fabrication of a room-temperature H2S gas sensor based on PPy/WO3 nanocomposite films by *in-situ* photopolymerization. *Sens. Actuat. B Chem.* 193, 637–643. doi: 10.1016/j.snb.2013.12.027

Tang, J., Liu, F., Zhang, X., Meng, Q., and Zhou, J. (2012). Partial discharge recognition through an analysis of SF6 decomposition products part 1: decomposition characteristics of SF6 under four different partial discharges. *IEEE Trans. Dielectr. Electr Insul.* 19, 29–36. doi: 10.1109/TDEI. 2012.6148499

Tang, J., Zeng, F., Pan, J., Zhang, X., Yao, Q., He, J., et al. (2013). Correlation analysis between formation process of SF6 decomposed components and partial discharge qualities. *IEEE Trans. Dielectr. Electr. Insul.* 20, 864–875. doi: 10.1109/TDEI.2013.6518956

Vanbrunt, R. J., and Herron, J. T. (1990). Fundamental processes of SF6 decomposition and oxidation in glow and corona discharges. *IEEE Trans. Electr. Insul.* 25, 75–94. doi: 10.1109/14.45235

Wan, Q., Xu, Y., Chen, X., and Xiao, H. (2018). Exhaled gas detection by a novel Rh-doped CNT biosensor for prediagnosis of lung cancer: a DFT study. *Mol. Phys.* 116, 2205–2212. doi: 10.1080/00268976.2018.1467057

Xu, Z., Duan, G., Li, Y., Liu, G., Zhang, H., Dai, Z., et al. (2014). CuO-ZnO micro/nanoporous array-film-based chemosensors: new sensing properties to H2S. *Chem. A Eur. J.* 20, 6040–6046. doi: 10.1002/chem.2013 04722

Zhang, D., Wu, J., Li, P., and Cao, Y. (2017). Room-temperature SO2 gas sensing properties based on metal-doped MoS2 nanoflower: an experimental and density functional theory Investigation. *J. Mater. Chem. A* 5, 20666–20677. doi: 10.1039/C7TA07001B

Zhang, H., Feng, J., Fei, T., Liu, S., and Zhang, T. (2014). SnO2 nanoparticles-reduced graphene oxide nanocomposites for NO2 sensing at low operating temperature. *Sens. Actuat. B Chem.* 190, 472–478. doi: 10.1016/j.snb.2013.08.067

Zhang, J., Liu, X., Wang, L., Yang, T., Guo, X., Wu, S., et al. (2011). A simple one-pot strategy for the synthesis of ternary reduced graphite oxide/SnO2/Au hybrid nanomaterials. *Carbon* 49, 3538–3543. doi: 10.1016/j.carbon.2011.04.053

Zhang, X., Meng, F., and Yang, B. (2013). Use of hydroxyl-modified carbon nanotubes for detecting SF6 decomposition products under partial discharge in gas insulated switchgear. *IEEE Trans. Dielectr. Electr Insul.* 18, 2246–2253. doi: 10.1109/TDEI.2013.6678876

Zhang, X., Yu, L., Wu, X., and Hu, W. (2015). Experimental sensing and density functional theory study of H2S and SOF2 adsorption on Au-Modified graphene. *Adv. Sci.* 2:150010111. doi: 10.1002/advs.201 500101